

## Baryon Acoustic Oscillations analyses with Density-Split Statistics

TENGPENG XU <sup>1,2</sup> YAN-CHUAN CAI <sup>3</sup> YUN CHEN <sup>1,2</sup> MARK NEYRINCK <sup>4,5</sup> LIANG GAO <sup>1</sup> AND QIAO WANG <sup>1,2</sup>

<sup>1</sup>*Key Laboratory for Computational Astrophysics, National Astronomical Observatories, Chinese Academy of Sciences  
Beijing 100101, China*

<sup>2</sup>*College of Astronomy and Space Sciences, University of Chinese Academy of Sciences  
Beijing, 100049, China*

<sup>3</sup>*Institute for Astronomy, University of Edinburgh, Royal Observatory  
Blackford Hill, Edinburgh, EH9 3HJ, UK*

<sup>4</sup>*Department of Physics and Astronomy, University of Denver, Denver, CO 80210, USA*

<sup>5</sup>*Blue Marble Space Institute of Science, Seattle, WA 98104, USA*

### ABSTRACT

Accurate modeling for the evolution of the Baryon Acoustic Oscillations (BAO) is essential for using it as a standard ruler to probe cosmology. We explore the non-linearity of the BAO in different environments using the density-split statistics and compare them to the case of the conventional two-point correlation function (2PCF). We detect density-dependent shifts for the position of the BAO with respect to its linear version using halos from N-body simulations. Around low/high-densities, the scale of the BAO expands/contracts due to non-linear peculiar velocities. As the simulation evolves from redshift 1 to 0, the difference in the magnitude of the shifts between high- and low-density regions increases from the sub-percent to the percent level. In contrast, the scale of the BAO does not evolve in the total 2PCF in the same redshift range. The width of the BAO around high density regions increases as the universe evolves, similar to the known broadening of the BAO in the 2PCF due to non-linear evolution. In contrast, the width is smaller and stable for low density regions. We discuss possible implications for the reconstructions of the BAO in light of our results.

*Keywords:* Large-scale structure of the universe(902) — Baryon acoustic oscillations(138) — N-body simulations(1083)

### 1. INTRODUCTION

Baryon Acoustic Oscillations (BAO) represents the sound waves in the primordial baryon-photon plasma before recombination due to the interactions between gravity, provided by the total matter, and the pressure, provided by baryons. The largest scale at which sound waves can propagate by the time of recombination defines the sound horizon. After recombination, the scale of the sound horizon is frozen into the baryon density fluctuations (and hence the matter density fluctuations) in comoving units, denoted as  $r_d \sim 147 \text{ Mpc} \sim 100 \text{ Mpc}/h$ .  $r_d$  represents the sound horizon at the drag epoch ( $z_d$ ), when baryons are released from the Compton drag of the photons, determined by the ratio

of baryon to matter densities (Eisenstein & Hu 1998; Hu & Sugiyama 1996). The sound horizon has been measured precisely by WMAP and Planck through the temperature fluctuations of the cosmic microwave background (e.g. Bennett et al. 2013; Planck Collaboration et al. 2020). These acoustic oscillations, imprinted in the matter density with a comoving scale of  $r_d$ , result in a peak in the two-point correlation function of matter, serving as one of the most precise standard rulers in cosmology for measuring cosmological distances. In the last few decades, generations of surveys such as 2dFGRS, 6dFGS, SDSS, BOSS, eBOSS and DESI had used it to set constraints on cosmological parameters (Cole et al. 2005; Beutler et al. 2011; Eisenstein et al. 2005; Ross et al. 2015; Alam et al. 2017, 2021; Zarrouk et al. 2018; DESI Collaboration et al. 2024).

However, the position of the BAO is not fixed after recombination in comoving coordinates, which we assume

throughout. Non-linear growth of structure is expected to cause the location of the BAO to shift, typically at the sub-percent level; the width of the BAO is broadened relative to its initial state (e.g. [Crocce & Scoccimarro 2008](#); [Seo et al. 2008, 2010](#); [Orban & Weinberg 2011](#)). The broadening of the peak of the BAO can be thought of as the consequence of peculiar velocities around high and low density regions pulling the BAO in opposite directions, usually in a non-symmetric way. This weakens the significance of the BAO peak and complicates the modeling. Significant effort has been made to reconstruct the BAO to reinstall the information from its initial conditions. A common practice is to perform reconstructions by using the observed late-time positions of galaxies, estimate their velocities and move the galaxies back to their initial conditions (e.g. [Eisenstein et al. 2007](#); [Noh et al. 2009](#); [Padmanabhan et al. 2009](#); [Seo et al. 2010](#); [White 2015](#); [Schmittfull et al. 2015](#); [Wang et al. 2017](#); [Yu et al. 2017](#); [Mao et al. 2021](#); [von Hausegger et al. 2022](#); [Nikakhtar et al. 2022, 2023](#); [Chan et al. 2024](#)). Indeed, reconstructions applied to cubic-box simulations were shown to substantially reduce the broadening and nonlinear shifts of the BAO, but this may not always be the case in real observations with complicated survey masks (e.g. [Anderson et al. 2012](#)), or when the shot-noise level of the galaxy sample is high ([White 2010](#); [Wang & Pen 2019](#); [Seo et al. 2022](#)). In principle, if we can track the non-linear evolution of the BAO precisely, forward modeling can also be applied to extract cosmological information (e.g. [Babić et al. 2022](#)). In addition, introducing environmental-dependence weights for the reconstruction by up-weighting under-dense environments has been demonstrated to help sharpening the peak of the BAO ([Achitouv & Blake 2015](#)). It has also been shown that reconstructions sharpen the BAO around voids more than for the 2PCF of mock galaxies ([Zhao et al. 2020](#)). All these indicate potential benefits for understanding the environmental dependence for the non-linear evolution of the BAO, which is the focus of our study.

In light of the above, we take a slightly different approach to analyze the BAO. We will identify density fluctuations in the late-time Universe around which the scale of the BAO may have changed relative to its initial position, and analyze them separately. This was first proposed by [Neyrinck et al. \(2018\)](#) using a similar concept, which they call sliced correlation functions.

In this paper, we will take a step forward to perform BAO analyses with halos from the QUIJOTE simulations ([Villaescusa-Navarro et al. 2020](#)). We will use the density-split clustering (DS), or conditional correlation functions for the analysis ([Paillas et al. 2021, 2023](#)). We

will split the two-point correlation function into a series of cross-correlation functions to be conditioned on local densities of different depth. By doing this, we aim to identify the possible expansion and contraction of the BAO scale around different density environments, with the perspective of tracking the broadening of the BAO. In this method, the 2PCF can be seen as a composition of the whole spectrum of cross-correlation functions. In addition, recent studies with DS-clustering have suggested significant gain of cosmological information over two-point correlation functions ([Paillas et al. 2023, 2024](#)). We would like to explore if BAO analyses with DS-clustering have any significant impact in the error budget compared to two-point statistics. We will address both the shifts and the broadening of the BAO together by performing error analyses.

The paper is organized as follows. In Section 2 we introduce the QUIJOTE simulations, the halo catalogs used in this work, and describing the measurements of the density-split clustering. We present our models and their parameters for the correlation functions in Section 3. Our BAO analyses are presented in Section 4. We provide discussions and the main conclusions in Section 5.

## 2. DENSITY-SPLIT CLUSTERING MEASUREMENTS FROM SIMULATIONS

### 2.1. *The QUIJOTE simulation*

The QUIJOTE project ([Villaescusa-Navarro et al. 2020](#)) comprises a series of N-body simulations aimed at assessing the information content in cosmological observables, spanning a wide range of values around its fiducial cosmology, which is consistent with the latest Planck constraints. The parameters of the fiducial cosmology are set as follows:  $\Omega_m = 0.3175$ ,  $\Omega_b = 0.049$ ,  $h = 0.6711$ ,  $n_s = 0.9624$ ,  $\sigma_8 = 0.834$ ,  $M_\nu(\text{eV}) = 0$ , and  $w = -1$ . There are 15,000 realizations of the fiducial cosmology encompassed in the QUIJOTE simulations, providing a substantial dataset for the computation of covariance matrices. Dark matter particles and halos catalogs obtained with a Friends-of-Friends algorithm ([Davis et al. 1985](#)) are provided. In our work, we utilized the dark matter halo catalogs with a minimal halo mass of  $1.31 \times 10^{13} M_\odot/h$  from 1000 realizations of the simulations. Table. 1 summarizes some properties of the catalogs. We focus on the data at redshifts  $z = 0, 0.5$ , and 1 where most galaxy redshift surveys can cover.

### 2.2. *Measurements of clustering*

We follow the algorithm presented in [Paillas et al. \(2021, 2023\)](#) to split the halo field into density bins. We apply spherical top-hat smoothing with a radius

snapshots ID	8000	8001	8002	8003	8004	...	8999	average number	standard deviation
$z = 1.0$	195633	195604	195236	195747	195096	...	195805	195575.9	362.9
$z = 0.5$	308580	310607	309485	309694	309832	...	309929	309426.1	476.6
$z = 0.0$	406728	407631	406226	406035	407212	...	406990	406764.2	642.8

**Table 1.** The samples of dark matter halos from the QUIJOTE simulation used for our analyses. They have the minimal halo mass  $M_{\min} = 1.31 \times 10^{13} M_{\odot}/h$  at  $z = 0, 0.5$  and 1.

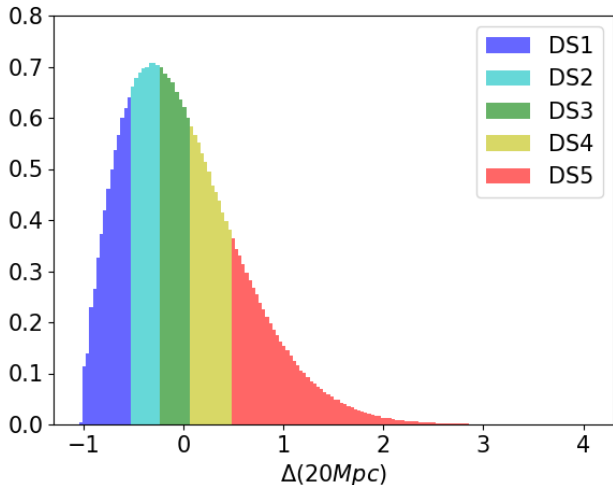


**Figure 1.** The normalized PDF of the halo number density contrast smoothed with a spherical top-hat window of the radius  $R = 20 \text{ Mpc}/h$ . Regions of increasing local densities, corresponding to DS<sub>1</sub> to DS<sub>5</sub> are shown in different colors. The auto-correlations of these DS centers, and their cross-correlations with halos are presented in Fig. 2. These are the basis for the density-split clustering analyses described in the paper. The measurement was conducted for one box of the QUIJOTE simulation at  $z = 0$ .

of  $R = 20h^{-1}\text{Mpc}$  to the halo number density field, and measure the smoothed density at random locations (called DS centers, for centers of top-hat smoothing spheres) of the simulation box. Note that a DS center does not usually correspond to the location of a halo. The number of randoms in each box are set to be  $M$  times the number of halos,  $N_{\text{random}} = M \times N_{\text{halos}}$ , where  $M$  is the number of density bins we are going to use for the split. This is to insure fair comparisons with the 2PCF (Paillas et al. 2023). This is equivalent to counting the number of halos around the random positions to measure the halo number density fluctuations within  $R$ :

$$\Delta(R) = \frac{\rho(< R)}{\bar{\rho}} - 1, \quad (1)$$

where  $\bar{\rho}$  is the mean halo density of the entire simulated box. The probability density function (PDF) of the density contrasts for a single realization at  $z = 0$  is shown in Fig. 1.

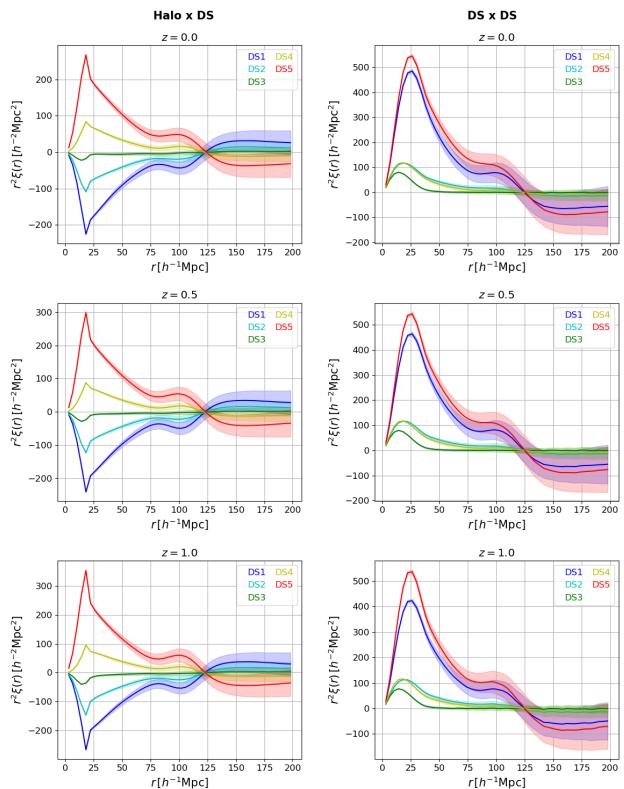


**Figure 2.** Measurements from the QUIJOTE simulations for the cross-correlation functions between halos and density-split centers (Halo  $\times$  DS, left panels) and the auto-correlation functions of density-split centers (DS  $\times$  DS, right panels). The top, middle and bottom panels show the results from redshifts  $z = 0, 0.5$  and 1, respectively. Solid lines are the averages from 1000 realizations of QUIJOTE simulations for the fiducial cosmology, with their errors shown in shaded regions. Different colors indicate the auto- and cross-correlations for different DS<sub>*i*</sub> ( $i=1, 2, 3, 4, 5$ ).

Next, we divide the DS centers equally into  $M$ -bins and by default, five quintiles, naming them from DS<sub>1</sub> to DS<sub>5</sub>. Hence DS<sub>1</sub> corresponds to under-density regions, while DS<sub>5</sub> corresponds to over-density regions. We also repeat our analyses with  $M = 10$  with results presented in Appendix B.

Fig. 3 display the distribution of halos, DS<sub>1</sub> and DS<sub>5</sub> centers in a two-dimensional slice with a thickness of 50

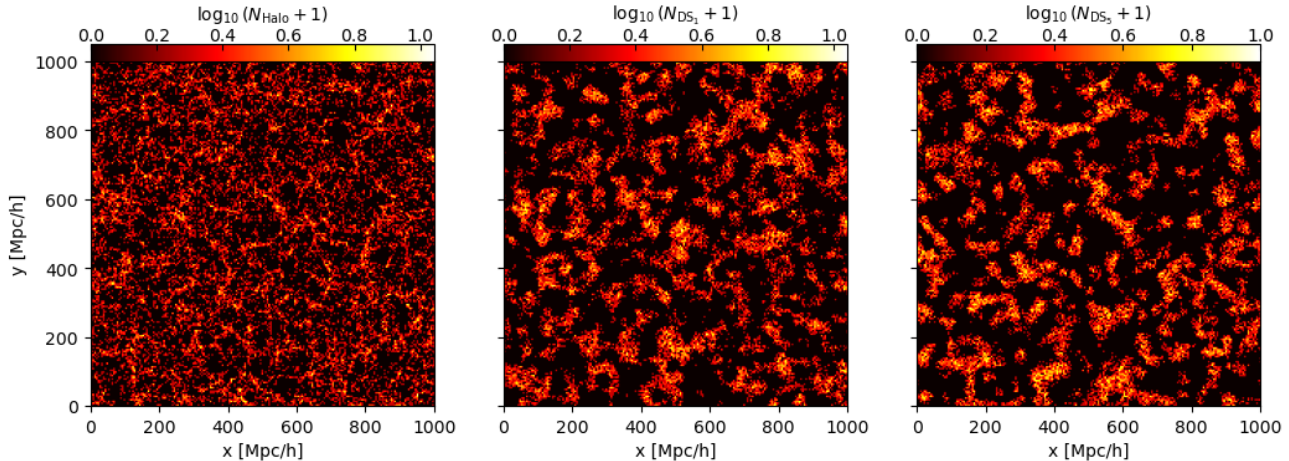


**Figure 3.** **Left:** A 2D slice of halo number counts from one realization of the QUIJOTE simulations. The thickness of the slice is 50 Mpc/h, with each pixel of the size of 5 Mpc/h  $\times$  5 Mpc/h. **Middle:** Number counts of DS<sub>1</sub> centers (the most under-dense regions) selected from filtering the 3D halo number density field with a spherical top-hat filter of the radius of 20Mpc/h (see Section 2.2 and Fig. 1 for more details). **Right:** Similar to the middle panel but showing the number counts of DS<sub>5</sub> centers (the most over-dense regions). It can be observed that the distribution of DS<sub>1</sub> mostly corresponds to the void regions in the halo distribution, whereas the DS<sub>5</sub> distribution is largely complementary to that of DS<sub>1</sub>, occupying high-density regions.

Mpc/h at redshift  $z = 0$  (corresponding to the three subplots from left to right, respectively). We can visually observe that the distribution of DS<sub>1</sub> mostly corresponds to the void regions in the halo distribution, whereas the DS<sub>5</sub> distribution is largely complementary to that of DS<sub>1</sub>.

With these DS centers, we utilize the `pycorr` software package (Sinha & Garrison 2019; Sinha & Garrison 2020) to calculate the cross-correlation functions between DS<sub>1</sub>-DS<sub>5</sub> centers and dark matter halos for the 1000 Realizations at  $z = 0, 0.5, 1.0$ . We also compute the auto-correlation functions of DS<sub>1</sub>-DS<sub>5</sub> centers. In the following text, we denote the cross-correlation functions as “Halo  $\times$  DS” or  $\xi_i^{\text{qh}}$ , and the auto-correlation functions of DS<sub>*i*</sub> as “DS  $\times$  DS” or  $\xi_i^{\text{qq}}$ , where “q” and “h” are abbreviations for “quintile” and “halo”, respectively. The measurements of these correlation functions are shown in Fig. 2.

### 3. THEORETICAL MODELS OF CORRELATION FUNCTIONS

For the model, we first utilize the `Nbodykit` package (Hand et al. 2018) to generate the linear power spectrum and the corresponding correlation functions at  $z = 0, 0.5$  and 1.0 based on the same fiducial cosmology of the QUIJOTE simulations. We use the sideband algorithm (Kirkby et al. 2013) to decompose the correlation function into two parts: one that exclusively contains the BAO peak ( $\xi_{\text{peak}}(r)$ ) and another that represents the smooth portion without the BAO peak ( $\xi_{\text{smooth}}(r)$ ). We then Fourier transform these components to obtain the corresponding power spectra,  $P_{\text{peak}}(k)$ , and  $P_{\text{smooth}}(k)$ .

Subsequently, we can calculate the quasi-linear power spectrum as:

$$P_{\text{QL}}(k; \sigma) = P_{\text{smooth}}(k) + \exp\left(-\frac{k^2 \sigma^2}{2}\right) P_{\text{peak}}(k), \quad (2)$$

where  $\sigma$  is the BAO peak’s non-linear damping term (referred to as the BAO width parameter in the following text). Therefore, we can express the tracer biased power spectrum as given by

$$\hat{P}(k; b_1, b_2, \sigma) = b_1 b_2 P_{\text{QL}}(k; \sigma), \quad (3)$$

where  $b_1$  and  $b_2$  represent the biases of the two tracers of interest e.g.,  $b_{\text{halo}}$  and  $b_{\text{DS}_i}$  in the context of this study. We obtain the corresponding two-point correlation functions  $\hat{\xi}(r; b_1, b_2, \sigma)$  through Fourier transformation of the model. Finally, we introduce the scale dilation parameter  $\alpha$  for the distortions to the correlations due to assuming a cosmology which is different from the fiducial one (Alcock & Paczynski 1979; Ballinger et al. 1996). In general, the scale dilation parameters for the line-of-sight distance and the transverse distance are:

$$\alpha_{\parallel} = \frac{[D_{\text{H}}(z)/r_{\text{d}}]}{[D_{\text{H}}(z)/r_{\text{d}}]_{\text{fid}}} \quad (4)$$

$$\alpha_{\perp} = \frac{[D_{\text{M}}(z)/r_{\text{d}}]}{[D_{\text{M}}(z)/r_{\text{d}}]_{\text{fid}}}, \quad (5)$$

where  $D_{\text{H}}$  and  $D_{\text{M}}$  are the Hubble distance and the comoving angular diameter distance at  $z$  respectively. These parameters is expected to provide the main cosmological constraints using the BAO. In this work, we focus on the possible shifts of the BAO positions, and so



we do not include redshift space distortions in our analyses. Therefore, the correlation functions are isotropic, so do the AP distortions, meaning that  $\alpha_{\parallel} = \alpha_{\perp}$ , where we denote as  $\alpha$  in the following text. The theoretical model of the correlation function is given as:

$$\xi_{\text{th}}(r; b_1, b_2, \alpha, \sigma) = \hat{\xi}(\alpha * r; b_1, b_2, \sigma). \quad (6)$$

Following the same notations introduced in Section 2.2,  $\xi_i^{\text{qh}}(r; b_{\text{halo}|DS_i}, b_{DS_i}, \alpha_i^{\text{qh}}, \sigma_i^{\text{qh}})$  represents the modeled cross-correlation function between dark matter halos and  $DS_i$  centers, where  $b_{\text{halo}|DS_i}, b_{DS_i}, \alpha_i^{\text{qh}}, \sigma_i^{\text{qh}}$  are free parameters, and  $i = 1, 2, \dots, 5$ . The same applies to the auto-correlation function of  $DS_i$  centers,  $\xi_i^{\text{qq}}(r; b_{DS_i}, \alpha_i^{\text{qq}}, \sigma_i^{\text{qq}})$ , and the auto-correlation function of dark matter halos,  $\xi^{\text{hh}}(r; b_{\text{halo}}, \alpha^{\text{hh}}, \sigma^{\text{hh}})$ . It is noteworthy that, in this study, the halo bias in the cross-correlation functions between dark matter halos and  $DS_i$  centers (denoted as  $b_{\text{halo}|DS_i}$ ) and the halo bias in the auto-correlation functions of dark matter halos (denoted as  $b_{\text{halo}}$ ) are considered as distinct free parameters. This allows us to explore potential disparities between the halo bias around  $DS_i$  centers and the global halo bias.

The  $\alpha$  parameter is a correction factor for the true cosmic distance relative to the fiducial cosmic distance. It also reflects deviations from the real position of the BAO relative to the reference cosmology. We treat  $\alpha$  of different correlation functions to be independent free parameters, with  $\alpha^{\text{hh}}$  for the halo clustering,  $\alpha_i^{\text{qh}}$  for DS-Halo cross-correlations, and  $\alpha_i^{\text{qq}}$  for DS-DS auto-correlations. From the definition, when  $\alpha > 1$ , the measured correlation function exhibits compression along the  $r$  axis, and so the BAO scale is smaller than in the fiducial cosmology. Conversely, when  $\alpha < 1$ , the opposite occurs. Only when  $\alpha = 1$ , there is no deviation between the measured BAO peak position and that of the reference universe.

In our analyses, the fiducial cosmology assumed is also the true cosmology, and so any deviation of  $\alpha$  from 1 must come from non-linear evolution. We will call it the BAO shift parameter in the rest of the paper. The level of deviation for  $\alpha$  for the 2PCF or power spectrum has been known to be at the sub-percent level at the late-time Universe (e.g. Crocce & Scoccimarro 2008; Seo et al. 2008, 2010; Orban & Weinberg 2011). With density-split clustering, the BAO scale around different background densities may shift differently, and the possible deviation of  $\alpha$  from 1 may become more obvious. In this work, we focus on the two most extreme densities –  $DS_5$  and  $DS_1$ , corresponding to the highest and lowest density fields. Guided by Neyrinck et al. (2018), these largest density perturbations may cause the scale of the BAO to have the most significant shift. We will

perform fitting with the model presented above with the measurements presented in section 2 to investigate this.

#### 4. MCMC FITTING FOR BAO POSITIONS

We employ the Markov Chain Monte Carlo (MCMC) method to constrain parameters in the correlation function model, utilizing the `emcee` software package (Foreman-Mackey et al. 2013). For any of the correlation functions,  $\xi^{\text{hh}}, \xi_i^{\text{qh}}$  or  $\xi_i^{\text{qq}}$ , the log-likelihood can be computed by comparing the theoretical data vector  $\xi_{\text{th}}$  with the measured data vector  $\xi_{\text{sim}}$  obtained from simulations:

$$\ln \mathcal{L} = -\frac{1}{2} \chi^2, \quad (7)$$

$$\chi^2 = (\xi_{\text{sim}} - \xi_{\text{th}}) \mathbf{C}^{-1} (\xi_{\text{sim}} - \xi_{\text{th}})^{\text{T}}. \quad (8)$$

For the data vector  $\xi_{\text{sim}}$ , we take the average over the measurements from the 1000 simulations. The covariance matrix  $\mathbf{C}$  is also computed using the 1000 simulation boxes of the fiducial cosmology:

$$\mathbf{C} = \frac{1}{N_{\text{sim}} - 1} \sum_{k=1}^{N_{\text{sim}}} (\xi_{\text{sim},k} - \bar{\xi}_{\text{sim}})^{\text{T}} (\xi_{\text{sim},k} - \bar{\xi}_{\text{sim}}), \quad (9)$$

where  $N_{\text{sim}} = 1000$ . Since the possible shift of the BAO peak position is expected to be small, we would like to reduce random errors as far as possible. We scaled down the covariance matrix by a factor of 1/100, which corresponds to reducing the error bars of each data point to one-tenth of their original sizes. This is equivalent to increasing the volume of the simulated box by a factor of 100, namely, the new box has a side length of approximately  $1 \text{ Gpc}/h \times 100^{1/3} \approx 4.6 \text{ Gpc}/h$ . For the fitting, we use the range of scales from  $80 \text{ Mpc}/h$  to  $180 \text{ Mpc}/h$  to encompass the co-moving BAO scale ( $r \sim 100 \text{ Mpc}/h$ ), and make linear binning for the data with the bin-width of  $4 \text{ Mpc}/h$ . We have compiled the parameter constraint results for all the correlation functions described above in Table 2, and present the full posterior distributions for all parameters in the Appendix A. Next, we will proceed with a detailed analysis of each parameter.

##### 4.1. BAO constraints from halo-halo correlations

The fitted results for the halo-halo correlation functions (2PCF) at  $z = 0, 0.5$  and  $1.0$  are shown in Fig. 5 (A). We can see that the model agrees very well with the measurements from simulations across the range of scales shown. Fig. 6 (A, B, C) presents the constrained for  $b_{\text{halo}}, \alpha^{\text{hh}}$  and  $\sigma^{\text{hh}}$ . We can see that at these three redshifts, the central values of the alpha parameter are approximately 0.36% greater than 1, and their

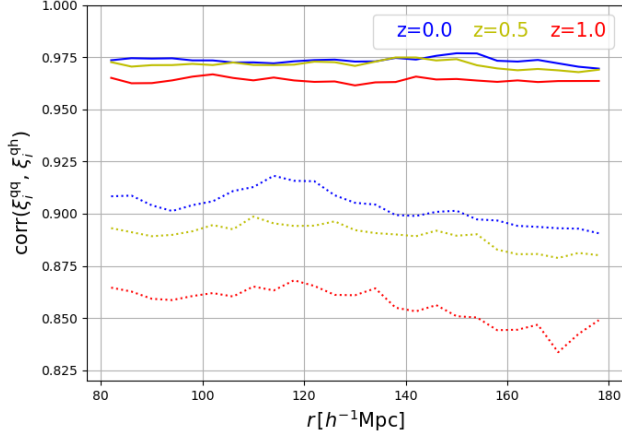


**Figure 4.** Comparing the correlation coefficients between the DS-DS and Halo-DS clustering at  $z = 0.0, 0.5$  and  $1.0$ , where the dotted lines represent  $DS_1$  (low densities) and the solid lines represent  $DS_5$  (high densities). These are derived from the full covariance matrix of  $[\xi^{\text{qq}}, \xi^{\text{qh}}]$ . The coefficients for  $DS_5$  are close to unity, suggesting that there is little gain of information when combining DS-DS with Halo-DS. The coefficients for  $DS_1$  are typically smaller than those for  $DS_5$ , suggesting more room for improvement when combining DS-DS with Halo-DS for under-dense regions.

differences from 1 all exceed the  $1\sigma$  level. The fact that  $\alpha^{\text{hh}} > 1$  suggests a contraction of the BAO scale relative to its linear version, consistent with previous studies (e.g. Crocce & Scoccimarro 2008; Seo et al. 2008, 2010; Urban & Weinberg 2011). This is expected as halos with the bias greater than 1 occupied over-dense regions. Overall, the co-moving BAO scales are consistent with no significant evolution within the redshift range of 1 to 0.

We can also see that the width of the BAO peak, as indicated by the parameter  $\sigma^{\text{hh}}$ , changes from about 5.0 to 7.7  $\text{Mpc}/h$  from  $z = 1$  to  $z = 0$ , a 50% increase. This is expected from non-linear evolution (e.g. Seo et al. 2008). In addition, the halo bias increases from  $\sim 1.4$  to  $\sim 2.8$  as the redshift increases from 0 to 1. This is expected as the density peaks corresponding to halos of the same low-mass cutoff become relatively rare at high- $z$ . Additionally, the bias parameter  $b_{\text{halo}}$  appears uncorrelated with the  $\alpha^{\text{hh}}$ , suggesting that the constraints on the BAO scale is unaffected by the amplitude of the clustering, as expected. All these indicate that our fitting pipeline works well for the 2PCF, and that there is no obvious shifts for the BAO scale in the 2PCF in this redshift range.

#### 4.2. BAO constraints from DS-clustering

For density-split clustering, we combine  $\xi_i^{\text{qq}}$  and  $\xi_i^{\text{qh}}$  together to obtain joint constraints for the shift pa-

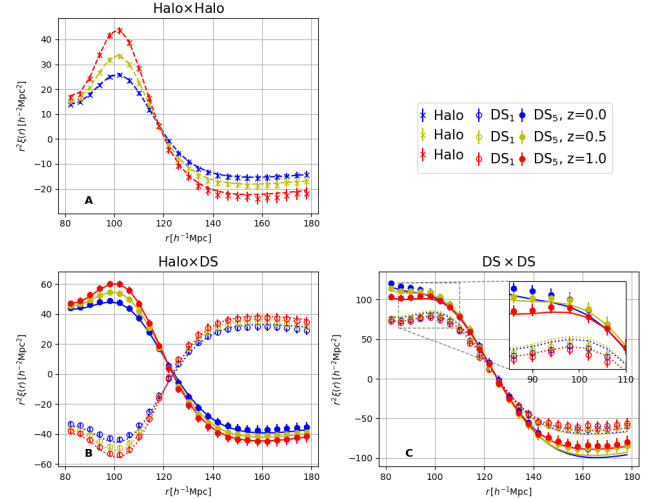


**Figure 5.** The best-fit results of the auto-correlation functions (Halo  $\times$  Halo), as well as the joint-fit results of the cross-correlation functions (Halo  $\times$  DS) and the auto-correlation functions (DS  $\times$  DS) at  $z = 0.0, 0.5$  and  $1.0$ . Points with error bars represent data obtained from simulated samples. The cross sign (‘x’) denotes Halo  $\times$  Halo correlation; solid and hollow circles are used to distinguish  $DS_5$  and  $DS_1$  for both Halo  $\times$  DS and DS  $\times$  DS correlation functions. Corresponding curves represent the best-fit models. Blue, yellow, and red lines correspond to  $z = 0.0, 0.5$  and  $1.0$ , respectively.

parameter. To account for the correlations between  $\xi_i^{\text{qq}}$  and  $\xi_i^{\text{qh}}$  at each redshift, we compute their joint covariance matrix and present the normalized correlation coefficients between  $\xi_i^{\text{qq}}$  and  $\xi_i^{\text{qh}}$  for both the  $DS_1$  and  $DS_5$  cases in Fig. 4. It can be seen from the figure that there is a strong correlation between  $\xi_i^{\text{qq}}$  and  $\xi_i^{\text{qh}}$ . However, the correlation coefficients are significantly smaller for  $DS_1$  than for  $DS_5$ . The cross-correlation functions are relatively more independent from their auto-correlation functions around under-dense regions than the case around high-density regions. This suggests that it is more valuable to combine  $\xi_i^{\text{qq}}$  and  $\xi_i^{\text{qh}}$  for  $DS_1$  – under-dense regions, than for  $DS_5$  – over-dense regions.

We can see from Fig. 5 (B, C) that the model provides excellent fits to the simulation measurements for both the auto-correlation functions (DS  $\times$  DS) and the cross-correlation functions (Halo  $\times$  DS) for  $DS_1$  and  $DS_5$  centers.

##### 4.2.1. Biases

Both the theoretical model of the auto-correlation functions  $\xi_i^{\text{qq}}(r; b_{DS_i}, \alpha_i^{\text{qq}}, \sigma_i^{\text{qq}})$  and the cross-correlation functions  $\xi_i^{\text{qh}}(r; b_{\text{halo}|DS_i}, b_{DS_i}, \alpha_i^{\text{qh}}, \sigma_i^{\text{qh}})$  have the parameter  $b_{DS_i}$ . Their combination is able to break the degeneracy between  $b_{\text{halo}}$  and  $b_{DS_i}$ , allowing independent

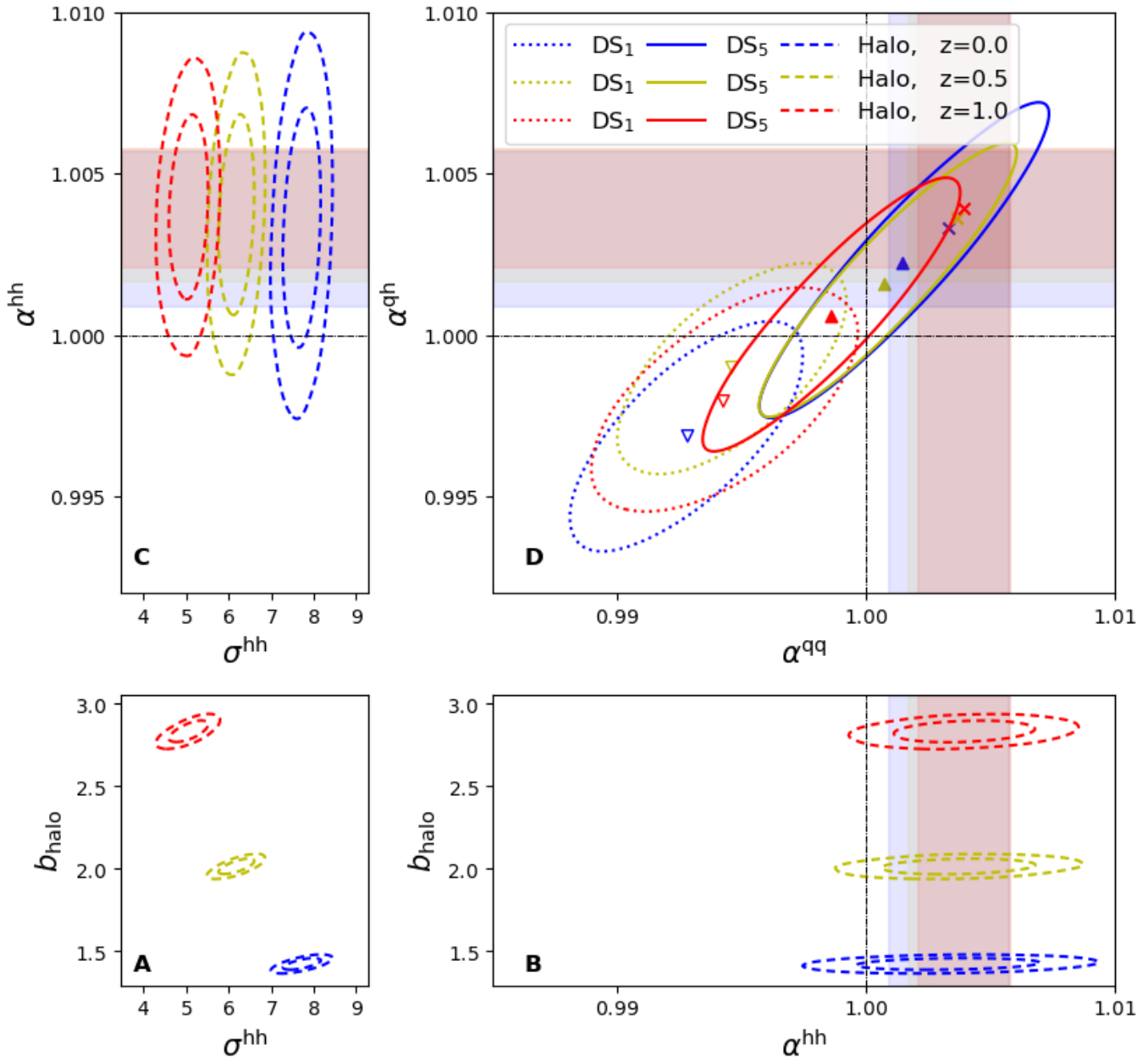


**Figure 6.** Panels A, B, C display the 2D posterior probability distributions of halo bias ( $b_{\text{halo}}$ ), the BAO shift parameter ( $\alpha^{\text{hh}}$ ), and the BAO width parameter ( $\sigma^{\text{hh}}$ ), obtained from MCMC fitting using halo auto-correlation functions. Large and small dashed contours represent the 68% and 95% confidence intervals, respectively. **Panel D** shows the 2D posterior probability distributions of the BAO shift parameters ( $\alpha^{\text{qh}}$  and  $\alpha^{\text{qq}}$ ) from joint constraints using DS  $\times$  DS and Halo  $\times$  DS correlation functions. Only the 68% confidence contours are shown, with DS<sub>1</sub> and DS<sub>5</sub> distinguished by dotted and solid lines, respectively. Best-fit  $\alpha^{\text{qh}}$ - $\alpha^{\text{qq}}$  values for DS<sub>1</sub> and DS<sub>5</sub> are marked with hollow-downward triangles and solid-upward triangles, respectively, while the best-fit  $\alpha^{\text{hh}}$  values are indicated with cross signs (“x”). **Overall:** Blue, yellow, and red lines correspond to  $z = 0.0, 0.5$  and  $1.0$ , respectively. The marginalized 68% confidence intervals of the  $\alpha^{\text{hh}}$  parameter are shown as shaded bands in Panels B, C, and D for comparison. Additionally, both horizontal and vertical dashed black lines represent the unshifted alpha parameter ( $\alpha = 1$ ).

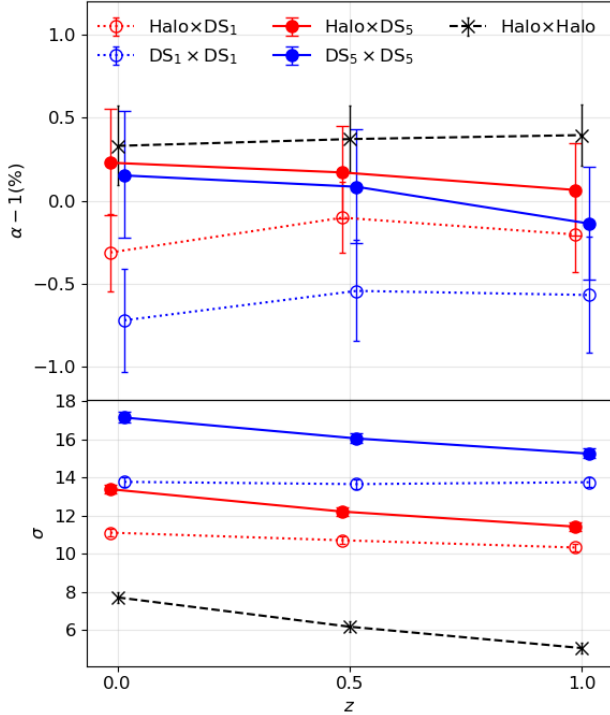


**Figure 7.** The marginalized constraints for the BAO shift parameter  $\alpha$  and width parameter  $\sigma$  at redshifts 0, 0.5, and 1. Black ‘x’ marks indicate the central values obtained from the halo auto-correlation function, while blue and red circles represent the central values obtained from the joint analysis of DS auto-correlation function and the Halo-DS cross-correlation function, respectively (hollow and solid circles distinguish DS<sub>1</sub> and DS<sub>5</sub>). The 68% confidence intervals for each parameter are displayed as error bars in the plot.

measurements for the halo bias in different environmental densities. As shown in Table 2, the biases of DS<sub>1</sub> differ significantly from those of DS<sub>5</sub>, with  $b_{\text{DS}_1} \sim -3.0$  and  $b_{\text{DS}_5} \sim 3.6$  at  $z = 0$ . These are significantly larger than the biases of the halos, suggesting that large-scale density fluctuations of these kinds are indeed rarer than the halos in our sample, but they are also more likely to be responsible for inducing non-linear evolution for the BAO. Furthermore, the biases for both DS<sub>1</sub> and DS<sub>5</sub> increase with redshift, similar to the evolution of the halo bias. Additionally, the halo biases in DS<sub>1</sub> and DS<sub>5</sub> environments are consistent with each other at the  $1\sigma$  level for all the three redshifts. They are also consistent with the global halo bias coming from the fitting with the 2PCF’s. These results suggest that to the linear order, the halos of the same mass are statistically similar in different environments, once the environmental factor is accounted for by the DS biases. This agrees with the theoretical expectations (Bardeen et al. 1986; Bond et al. 1991; Martino & Sheth 2009; Sheth & Tormen

$z$	0.0	0.5	1.0
$b_{\text{halo}}$	$1.425 \pm 0.023$	$2.015 \pm 0.031$	$2.832^{+0.042}_{-0.043}$
$\alpha^{\text{hh}}$	$1.0033^{+0.0025}_{-0.0024}$	$1.0037 \pm 0.0020$	$1.0039 \pm 0.0019$
$\sigma^{\text{hh}}$	$7.72 \pm 0.29$	$6.18^{+0.27}_{-0.28}$	$5.06^{+0.30}_{-0.31}$
$b_{\text{halo DS}_1}$	$1.435 \pm 0.023$	$2.041 \pm 0.033$	$2.851^{+0.048}_{-0.049}$
$b_{\text{DS}_1}$	$-3.02 \pm 0.05$	$-3.96^{+0.07}_{-0.06}$	$-4.83^{+0.09}_{-0.08}$
$\alpha_1^{\text{qq}}$	$0.9928 \pm 0.0031$	$0.9946^{+0.0031}_{-0.0030}$	$0.9943 \pm 0.0035$
$\alpha_1^{\text{qh}}$	$0.9969 \pm 0.0023$	$0.9990 \pm 0.0021$	$0.9980 \pm 0.0023$
$\sigma_1^{\text{qq}}$	$13.78^{+0.25}_{-0.24}$	$13.66 \pm 0.24$	$13.76^{+0.28}_{-0.27}$
$\sigma_1^{\text{qh}}$	$11.12 \pm 0.21$	$10.72^{+0.20}_{-0.19}$	$10.34^{+0.22}_{-0.21}$
$b_{\text{halo DS}_5}$	$1.423 \pm 0.020$	$2.016^{+0.028}_{-0.029}$	$2.817^{+0.043}_{-0.044}$
$b_{\text{DS}_5}$	$3.66 \pm 0.05$	$4.69 \pm 0.07$	$5.68 \pm 0.09$
$\alpha_5^{\text{qq}}$	$1.0015^{+0.0039}_{-0.0038}$	$1.0008 \pm 0.0034$	$0.9986 \pm 0.0034$
$\alpha_5^{\text{qh}}$	$1.0023 \pm 0.0032$	$1.0017 \pm 0.0028$	$1.0006^{+0.0028}_{-0.0027}$
$\sigma_5^{\text{qq}}$	$17.15^{+0.28}_{-0.26}$	$16.06^{+0.25}_{-0.24}$	$15.26^{+0.26}_{-0.25}$
$\sigma_5^{\text{qh}}$	$13.39^{+0.25}_{-0.24}$	$12.22 \pm 0.22$	$11.44^{+0.24}_{-0.23}$

**Table 2.** The central values of parameters along with their  $1\sigma$  errors from our BAO analyses fitted with  $\xi^{\text{hh}}$ ,  $\xi^{\text{qq}}$  and  $\xi^{\text{qh}}$ , after marginalizing over other parameters. Note that  $\xi^{\text{qq}}$  and  $\xi^{\text{qh}}$  of the same DS bins are combined into a single data vector for the fitting. The corresponding posterior distributions from which these values are derived are shown in Figs. 8 & 9.

1999) and findings from simulations (e.g. Alonso et al. 2015; Goh et al. 2019).

#### 4.2.2. BAO scales

Fig. 6(D) presents the 2D posterior distributions of the shift parameters  $\alpha_i^{\text{qq}}$  and  $\alpha_i^{\text{qh}}$  for DS<sub>1</sub> and DS<sub>5</sub>, along with  $\alpha^{\text{hh}}$  at redshifts  $z = 0.0, 0.5$ , and  $1.0$ . Additionally, to facilitate more intuitive comparisons at different redshifts, we present the central values of the BAO shift parameters  $\alpha$  with  $1\sigma$  error bars in Fig. 7. The complete posterior distributions for DS<sub>1</sub> and DS<sub>5</sub> are provided in Appendix A. Based on the information provided in Fig. 6, Fig. 7, and Table 2, the following insights can be intuitively gleaned:

- Both the  $\alpha^{\text{qq}}$  and the  $\alpha^{\text{qh}}$  parameters for DS<sub>5</sub> tend to be larger than those for DS<sub>1</sub>. This suggest that there are indeed contractions of the BAO scale around high-density regions compared to low-density regions.
- As the simulations evolves from redshift 1 to 0, the values of the  $\alpha^{\text{qq}}$  and  $\alpha^{\text{qh}}$  parameters for DS<sub>5</sub> increase, whereas DS<sub>1</sub> exhibits a mild opposite trend. Although



the best-fit  $\alpha^{\text{qq}}-\alpha^{\text{qh}}$  values for DS<sub>1</sub> at  $z = 0.5$  are slightly higher than those at  $z = 1$ , but they are consistent within the  $1\sigma$  confidence level, which is probably due to the insignificant evolution of the BAO shifts between redshift 1 and 0.5. The evolution becomes more obvious when we split the density field into 10 DS bins (see Fig. 10(c)). In the one-dimensional posterior distributions of the parameters at redshift 0, the difference between  $\alpha_1^{\text{qh}}$  and  $\alpha_5^{\text{qh}}$  nearly reaches  $1\sigma$ , while the difference between  $\alpha_1^{\text{qq}}$  and  $\alpha_5^{\text{qq}}$  exceeds  $1\sigma$ . The differences in their best-fit values are approximately 0.5% and 1%, respectively. The fact that the  $\alpha$  parameters around the low and high density regions evolve in opposite directions confirms the expansion/contraction of them in these two different environments due to non-linear evolution.

- The constrained results of parameters associated with the width of the BAO,  $\sigma_i^{\text{qh}}$  and  $\sigma_i^{\text{qq}}$ , are larger than those of the 2PCF version  $\sigma^{\text{hh}}$  (bottom panel of Fig. 7). This is mainly due to the convolution of the top-hat window function when splitting the densities. In addition, the width of the BAO for DS<sub>1</sub> is generally smaller than that for DS<sub>5</sub> (dotted versus solid lines at the bottom panel of Fig. 7), which is consistent with the results of (Achitouv & Blake 2015). This difference is possibly due to the smaller dynamical range of density for DS<sub>1</sub> than DS<sub>5</sub> (Fig. 1). They also exhibit different evolution between redshift one to zero. Both  $\sigma_5^{\text{qh}}$  and  $\sigma_5^{\text{qq}}$  increases with decreasing redshift, similar to the case of halo-halo clustering. However, both  $\sigma_1^{\text{qh}}$  and  $\sigma_1^{\text{qq}}$  remains stable across this redshift range.

The increase for the width of the BAO in the 2PCF as the universe evolve is expected from non-linear evolution. As halos reside on the peaks of the density field, they occupy a wide range of densities in the density PDF. The BAO's around different local densities evolve at different pace, resulting in a broadening of its width on average. In DS-clustering, DS<sub>5</sub> takes the positive tail of the non-Gaussian PDF of the density field (see Fig. 1), which also have a relatively wide dynamical range in density. Thus it can be expected that the width of the BAO around DS<sub>5</sub> centers follows a similar evolution trend as that of the 2PCF. For DS<sub>1</sub>, however, their local densities have a narrow dynamical range (see Fig. 1). The density perturbations are likely to evolve at a similar pace i.e., BAO's around under-dense regions will expand by a similar rate as they evolve. Their widths will therefore remain stable around these under-dense regions.

In summary, from the prospective of DS-clustering, BAO's around under- and over-dense regions evolve at different rates. By analyzing them together, such as the

case of the 2PCF, the situations in low- and high-density regions will be mixed up. The expansion from under-dense regions and the contraction from high-density regions will act together to broaden the width of the BAO.

## 5. DISCUSSION AND CONCLUSIONS

In this study, we have explored the possible deviation of the BAO scale in high-density and low-density regions due to non-linear evolution. We do so by analyzing the BAO with the density-split statistics using halos found in the QUIJOTE simulations. The density-split clustering starts from splitting the halo number density PDF smoothed at a 20 Mpc/ $h$ -scale into high- and low-density regions, called DS centers. We then measure the auto-correlations of these DS centers and their cross-correlations with the halos. We also compare the results with the standard analysis of the BAO using 2PCF. The main conclusions drawn from our analyses are as the follows:

For the scales of the BAO, using the the auto-correlation functions of DS centers and the cross-correlation functions between halos and DS centers, we observed a contraction (stretching) of the BAO scale in high-density (low-density) regions relative to its linear version, while the scale of the BAO in the auto-correlation function of halos remains stable in the same redshift range. At redshift zero, the difference in the BAO scale between high- and low-density regions is approximately 1%.

Two-point statistics can be seen as the composition of the whole spectrum of cross-correlations in DS-clustering. The sub-percent level shifts for the BAO in 2PCF is the sum of all the effects around high- and low-density regions in DS-clustering. Due to the opposite direction for the shifts of the BAO scale around high- and low-densities, a non-linear transformation for the density field which up-weight low-densities may compensate the contraction effect of the BAO around high-densities, and therefore reduce the shifts of the BAO in two-point statistics (McCullagh et al. 2013); a similar finding using the power spectrum, for general features, was explored by Neyrinck & Yang (2013).

For the width of the BAO, with density-split clustering, we find it to be larger than its 2PCF counterpart due to a convolution of a smoothing window function. The width is broadened by  $\sim 50\%$  between redshift 1 to 0 for the 2PCF. Similar evolution is seen for DS-clustering for the high-density regions. For the highest density bin in DS-clustering, DS<sub>5</sub>, it encloses the positive tail of the density PDF, which is more extended than the lowest density bin. The wide dynamical range of the local density, and the relatively strong

non-linearity around these high-densities may explain the relatively more rapid evolution for the width of the BAO around them. The width of the BAO does not appear to evolve for low-density regions, possibly due to having a similar evolution trend for the BAO around a narrow range of low-density environments i.e., the evolution of BAO's around voids may be relatively synchronized. This may also explain the fact that reconstructions by up-weighting low-density environments is beneficial in sharpening the BAO feature (Achitouv & Blake 2015), which is also seen in the reconstruction with mock galaxy catalogs (Zhao et al. 2020).

Our results agree qualitatively with the findings of (Neyrinck et al. 2018), but the magnitudes of the shifts are smaller. This is mainly because we are looking at a more realistic case where the density field is split into 5 quintiles. The local densities for DS<sub>1</sub> and DS<sub>5</sub> are not very extreme. Their density contrasts  $\delta$  differ from the mean by an order of 1. More significant shifts for the BAO scale is expected if one samples the density contrast of  $\delta \sim 10$  (Neyrinck et al. 2018). However, at the smoothing scale of 20 Mpc/h, density fluctuations of this amplitude are rare, and the measurements for the DS-clustering become noisy. With a smaller smoothing scale, one can increase the amplitude of density fluctuations while keeping the noise level down. However, having smaller scale fluctuations means weaker gravitational influence on the BAO, and hence smaller impacts on the BAO scale.

Nevertheless, with the default smoothing scale of 20 Mpc/h, we have repeated the analyses with 10 DS bins. Results are shown in Appendix B. In this case, DS<sub>1</sub> and DS<sub>10</sub> are more extreme low and high densities. We have indeed observe a more obvious trend for the expansion of the BAO scale for DS<sub>1</sub>, but the evolution for the BAO scale for DS<sub>10</sub> seems diminishing. The difference between these low and high densities becomes more extreme, reaching  $\sim 2\%$  at  $z = 0$ . Overall, the results from using 10 DS-bins remains qualitatively similar to the case of 5 bins.

In conclusion, we have detected clear deviations for the BAO features between the low- and high- density environments, both in terms of the shift of its scale and in its broadening. These results may provide theoretical grounds for better interpretations of the BAO beyond two-point statistics. Accurate modeling for the environmental dependents of these features, e.g. through density-split clustering, may allow us to better predict the non-linear behavior of the BAO, and thus extract more cosmological information.

We caution that with a focus on understanding the physics, our analyses are conducted in real space, but we anticipate the main conclusions to be similar in redshift space. If we take the perspective that the scenario in redshift space is a future universe in one of the three dimensions, the evolution effects of the BAO we have seen may be even stronger in redshift space. Indeed, this was seen for the shifts of the BAO in terms of the 2PCF (Seo et al. 2008).

1 This work has been supported by the National Natu-  
 2 ral Science Foundation of China (Nos. 11988101 and  
 3 12033008), the National Key Research and Develop-  
 4 ment Program of China (Nos. 2022YFA1602903 and  
 5 2023YFB3002501), the China Manned Space Project  
 6 (No. CMS-CSST-2021-A01), and the K. C. Wong Edu-  
 7 cation Foundation. YC acknowledges the support of the  
 8 UK Royal Society through a University Research Fellow-  
 9 ship. WQ acknowledges the supported by the Strate-  
 10 gic Priority Research Program of Chinese Academy of  
 11 Sciences, Grant No.XDB0500203. For the purpose of  
 12 open access, the author has applied a Creative Commons  
 13 Attribution (CC BY) licence to any Author Accepted  
 14 Manuscript version arising from this submission.

*Software:* `densitiesplit` (Paillas et al. 2021),  
`pycorr` (Sinha & Garrison 2019; Sinha & Garrison 2020),  
`Nbodykit` (Hand et al. 2018), `emcee` (Foreman-Mackey  
et al. 2013), `getdist` (Lewis 2019)

## APPENDIX

### A. COMPLETE POSTERIOR PROBABILITY DISTRIBUTIONS FROM THE DENSITY-SPLIT CLUSTERING

We display the 1D and 2D probability distributions of parameters of interest constrained by the auto-correlation and cross-correlation functions of DS<sub>1</sub> (Fig. 8) and DS<sub>5</sub> (Fig. 9) at  $z = 0, 0.5$  and 1 in this section. We split the halo density field into 5 bins, the default case for the paper. Results presented in Table 2 are derived from these figures.

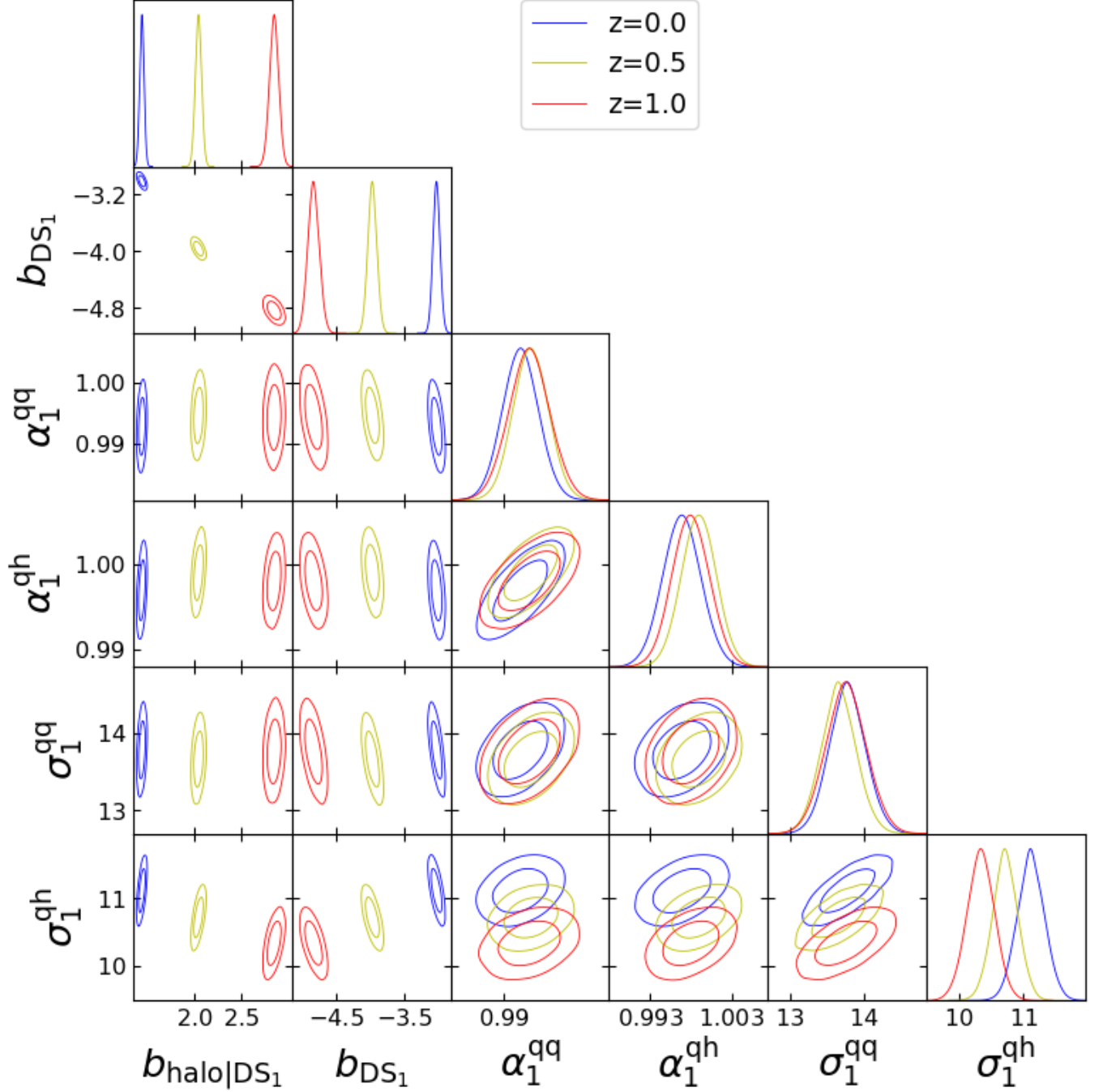


**Figure 8.** The 1D and 2D probability distributions of each pair of parameters constrained by the auto-correlation and cross-correlation functions of  $DS_1$  at  $z=0, 0.5$  and  $1$ . The contours correspond to 68% and 95% confidence levels. The density field is split into 5 density bins – the default choice of the paper. Results presented in Table 2 are derived from these.

## B. POSTERIOR PROBABILITY DISTRIBUTIONS FROM THE DENSITY-SPLIT CLUSTERING WITH 10 BINS

We repeat our analyses by splitting the halo density field into 10 density bins, with results shown in Figures 10(a) to 10(d). These can be compared with Figures 4 to 7 for the default case of having 5 density bins presented in the main part of the paper. The central values for the parameters with errors are presented in Table 3, to be compared with Table 2.

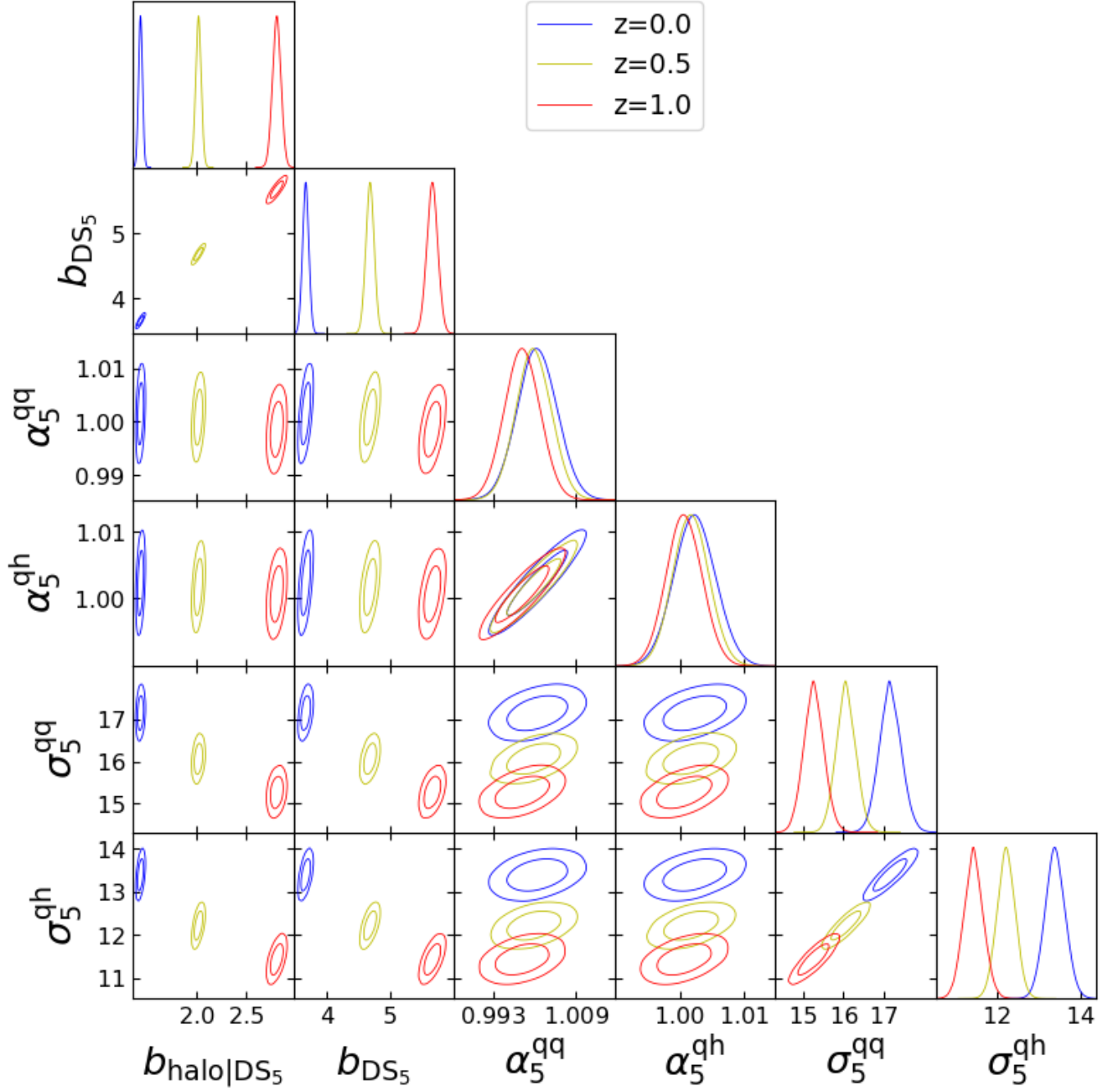
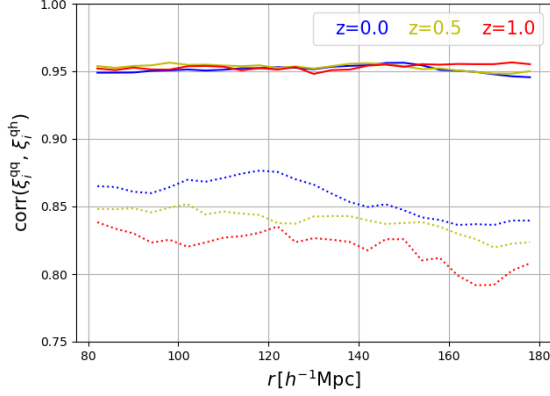
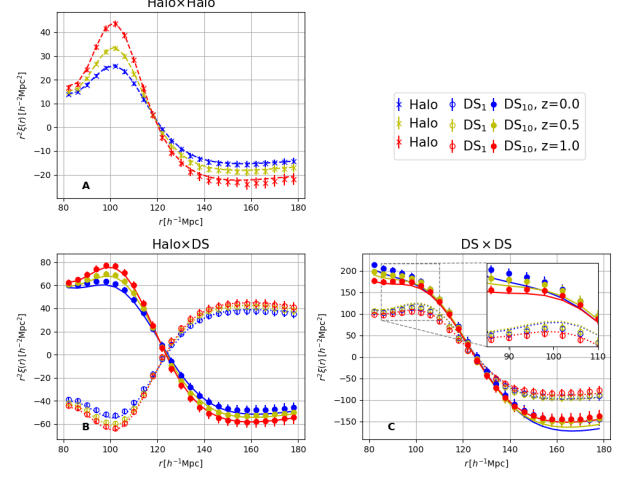


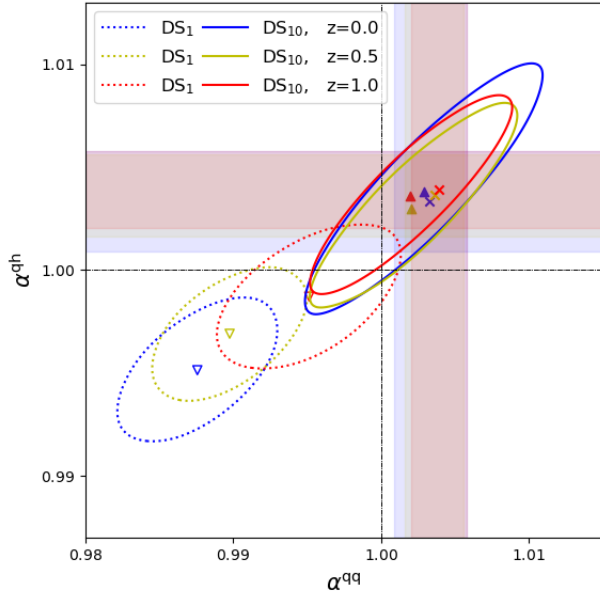
**Figure 9.** The 1D and 2D probability distributions of each pair of parameters constrained by the auto-correlation and cross-correlation functions of  $\text{DS}_5$  at  $z=0, 0.5$  and  $1$ . The contours correspond to 68% and 95% confidence levels. The density field is split into 5 density bins– the default choice of the paper. Results presented in Table 2 are derived from these.



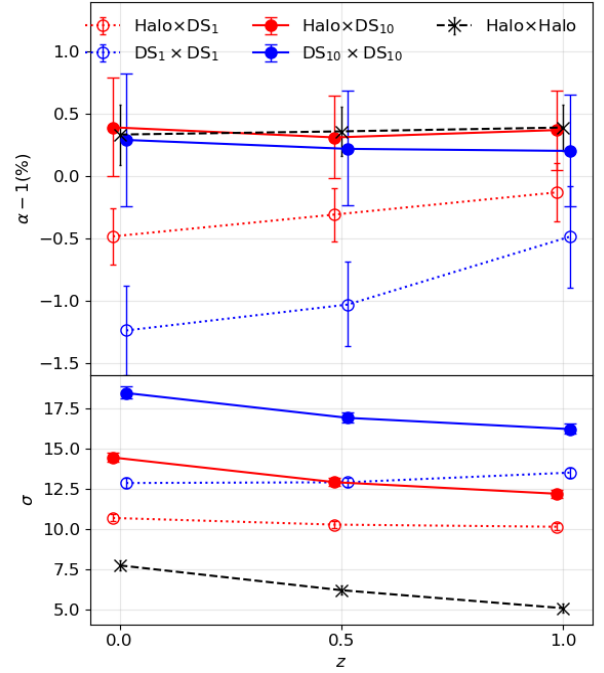
(a) For the 10 density bin case, comparing the correlation coefficients between the DS-DS and Halo-DS clustering at  $z = 0.0, 0.5$  and  $1.0$ , where the dotted lines represent  $DS_1$  and the solid lines represent  $DS_{10}$ . The results are similar to those with 5 density bins presented in Fig. 4, except that the magnitudes of the correlation coefficients are all smaller, and there is no significant evolution in the correlation coefficients for high-density regions as the redshift changes from 0 to 1.



(b) For the case of 10 density bins, the best-fit results of the auto-correlation functions (Halo  $\times$  Halo), as well as the joint fit results of the cross-correlation functions (Halo  $\times$  DS) and the auto-correlation functions (DS  $\times$  DS) at  $z = 0.0, 0.5$  and  $1.0$ . Similar to the 5 density bins case (Fig. 5), the correlation function models we used can well fit the measurements obtained from the simulation data.



(c) For the 10 density bin case, the 2D probability distributions of the BAO shift parameters ( $\alpha^{\text{qh}}$  and  $\alpha^{\text{qq}}$ ) from joint constraints using DS  $\times$  DS and Halo  $\times$  DS correlation functions, with the details similar to Fig. 6. As the redshift evolves from 1 to 0, the contraction of the BAO scale in high-density regions is insignificant, whereas the expansion in low-density regions is pronounced. At  $z = 0$ , the differences between high- and low-density regions is larger than the 5-bin case shown in Fig. 6.



(d) For the 10 density bin case, the marginalized constraints for the BAO shift parameter  $\alpha$  and width parameter  $\sigma$  at redshifts 0, 0.5, and 1. The evolution of the  $\alpha$  parameter with redshift is similar to the case of 5 density bins shown in Fig. 7, except that the evolution in high-density regions becomes less significant while the evolution in low-density regions becomes more pronounced. The evolution of the  $\sigma$  parameter is consistent with the case of 5 density bins, indicating that the width of the BAO peak in low-density regions is indeed stable in this redshift range.

**Figure 10.** Main results of density-split analysis with 10 density bins.



$z$	0.0	0.5	1.0
$b_{\text{halo}}$	$1.425 \pm 0.023$	$2.015 \pm 0.031$	$2.832 \pm 0.043$
$\alpha^{\text{hh}}$	$1.0034^{+0.0025}_{-0.0024}$	$1.0036 \pm 0.0020$	$1.0039 \pm 0.0019$
$\sigma^{\text{hh}}$	$7.72 \pm 0.29$	$6.18^{+0.27}_{-0.28}$	$5.06^{+0.29}_{-0.31}$
$b_{\text{halo} DS_1}$	$1.426^{+0.026}_{-0.027}$	$2.019 \pm 0.036$	$2.839^{+0.051}_{-0.052}$
$b_{DS_1}$	$-3.56 \pm 0.07$	$-4.68 \pm 0.09$	$-5.64 \pm 0.11$
$\alpha_1^{\text{qq}}$	$0.9876 \pm 0.0036$	$0.9897^{+0.0035}_{-0.0034}$	$0.9952 \pm 0.0041$
$\alpha_1^{\text{qh}}$	$0.9952 \pm 0.0023$	$0.9969 \pm 0.0021$	$0.9987 \pm 0.0023$
$\sigma_1^{\text{qq}}$	$12.85^{+0.30}_{-0.29}$	$12.90^{+0.30}_{-0.29}$	$13.50^{+0.32}_{-0.31}$
$\sigma_1^{\text{qh}}$	$10.68^{+0.22}_{-0.21}$	$10.26^{+0.21}_{-0.20}$	$10.13 \pm 0.22$
$b_{\text{halo} DS_{10}}$	$1.423 \pm 0.021$	$2.001^{+0.029}_{-0.030}$	$2.826^{+0.042}_{-0.043}$
$b_{DS_{10}}$	$4.83 \pm 0.07$	$6.10^{+0.09}_{-0.10}$	$7.45^{+0.12}_{-0.13}$
$\alpha_{10}^{\text{qq}}$	$1.0029 \pm 0.0053$	$1.0022^{+0.0046}_{-0.0045}$	$1.0020 \pm 0.0045$
$\alpha_{10}^{\text{qh}}$	$1.0039^{+0.0040}_{-0.0039}$	$1.0031^{+0.0033}_{-0.0032}$	$1.0037 \pm 0.0032$
$\sigma_{10}^{\text{qq}}$	$18.45^{+0.39}_{-0.36}$	$16.90^{+0.33}_{-0.31}$	$16.21^{+0.33}_{-0.31}$
$\sigma_{10}^{\text{qh}}$	$14.44^{+0.29}_{-0.28}$	$12.90^{+0.26}_{-0.25}$	$12.18^{+0.26}_{-0.25}$

**Table 3.** The central values of parameters along with their  $1\sigma$  errors from our BAO analyses using  $\xi^{\text{hh}}$ ,  $\xi^{\text{qq}}$  and  $\xi^{\text{qh}}$  for the case of  $M = 10$ , after marginalizing over other parameters. Note that  $\xi^{\text{qq}}$  and  $\xi^{\text{qh}}$  of the same DS bins are combined into a single data vector for the fitting. The results in this table are to be compared with the results for the case of 5 density bins shown in Table. 2.

## REFERENCES

- Achitouv, I., & Blake, C. 2015, *PhRvD*, 92, 083523, doi: [10.1103/PhysRevD.92.083523](https://doi.org/10.1103/PhysRevD.92.083523)
- Alam, S., Ata, M., Bailey, S., et al. 2017, *MNRAS*, 470, 2617, doi: [10.1093/mnras/stx721](https://doi.org/10.1093/mnras/stx721)
- Alam, S., Aubert, M., Avila, S., et al. 2021, *PhRvD*, 103, 083533, doi: [10.1103/PhysRevD.103.083533](https://doi.org/10.1103/PhysRevD.103.083533)
- Alcock, C., & Paczynski, B. 1979, *Nature*, 281, 358, doi: [10.1038/281358a0](https://doi.org/10.1038/281358a0)
- Alonso, D., Eardley, E., & Peacock, J. A. 2015, *MNRAS*, 447, 2683, doi: [10.1093/mnras/stu2632](https://doi.org/10.1093/mnras/stu2632)
- Anderson, L., Aubourg, E., Bailey, S., et al. 2012, *MNRAS*, 427, 3435, doi: [10.1111/j.1365-2966.2012.22066.x](https://doi.org/10.1111/j.1365-2966.2012.22066.x)
- Babić, I., Schmidt, F., & Tucci, B. 2022, *JCAP*, 2022, 007, doi: [10.1088/1475-7516/2022/08/007](https://doi.org/10.1088/1475-7516/2022/08/007)
- Ballinger, W. E., Peacock, J. A., & Heavens, A. F. 1996, *MNRAS*, 282, 877, doi: [10.1093/mnras/282.3.877](https://doi.org/10.1093/mnras/282.3.877)
- Bardeen, J. M., Bond, J. R., Kaiser, N., & Szalay, A. S. 1986, *ApJ*, 304, 15, doi: [10.1086/164143](https://doi.org/10.1086/164143)
- Bennett, C. L., Larson, D., Weiland, J. L., et al. 2013, *ApJS*, 208, 20, doi: [10.1088/0067-0049/208/2/20](https://doi.org/10.1088/0067-0049/208/2/20)
- Beutler, F., Blake, C., Colless, M., et al. 2011, *MNRAS*, 416, 3017, doi: [10.1111/j.1365-2966.2011.19250.x](https://doi.org/10.1111/j.1365-2966.2011.19250.x)
- Bond, J. R., Cole, S., Efstathiou, G., & Kaiser, N. 1991, *ApJ*, 379, 440, doi: [10.1086/170520](https://doi.org/10.1086/170520)
- Chan, K. C., Lu, G., & Wang, X. 2024, *MNRAS*, 529, 1667, doi: [10.1093/mnras/stae638](https://doi.org/10.1093/mnras/stae638)
- Cole, S., Percival, W. J., Peacock, J. A., et al. 2005, *MNRAS*, 362, 505, doi: [10.1111/j.1365-2966.2005.09318.x](https://doi.org/10.1111/j.1365-2966.2005.09318.x)
- Crocce, M., & Scoccimarro, R. 2008, *PhRvD*, 77, 023533, doi: [10.1103/PhysRevD.77.023533](https://doi.org/10.1103/PhysRevD.77.023533)
- Davis, M., Efstathiou, G., Frenk, C. S., & White, S. D. M. 1985, *ApJ*, 292, 371, doi: [10.1086/163168](https://doi.org/10.1086/163168)
- DESI Collaboration, Adame, A. G., Aguilar, J., et al. 2024, arXiv e-prints, arXiv:2404.03002, doi: [10.48550/arXiv.2404.03002](https://doi.org/10.48550/arXiv.2404.03002)
- Eisenstein, D. J., & Hu, W. 1998, *ApJ*, 496, 605, doi: [10.1086/305424](https://doi.org/10.1086/305424)
- Eisenstein, D. J., Seo, H.-J., Sirko, E., & Spergel, D. N. 2007, *ApJ*, 664, 675, doi: [10.1086/518712](https://doi.org/10.1086/518712)
- Eisenstein, D. J., Zehavi, I., Hogg, D. W., et al. 2005, *ApJ*, 633, 560, doi: [10.1086/466512](https://doi.org/10.1086/466512)
- Foreman-Mackey, D., Hogg, D. W., Lang, D., & Goodman, J. 2013, *PASP*, 125, 306, doi: [10.1086/670067](https://doi.org/10.1086/670067)
- Goh, T., Primack, J., Lee, C. T., et al. 2019, *MNRAS*, 483, 2101, doi: [10.1093/mnras/sty3153](https://doi.org/10.1093/mnras/sty3153)
- Hand, N., Feng, Y., Beutler, F., et al. 2018, *AJ*, 156, 160, doi: [10.3847/1538-3881/aadae0](https://doi.org/10.3847/1538-3881/aadae0)
- Hu, W., & Sugiyama, N. 1996, *ApJ*, 471, 542, doi: [10.1086/177989](https://doi.org/10.1086/177989)
- Kirkby, D., Margala, D., Slosar, A., et al. 2013, *JCAP*, 2013, 024, doi: [10.1088/1475-7516/2013/03/024](https://doi.org/10.1088/1475-7516/2013/03/024)
- Lewis, A. 2019, arXiv e-prints, arXiv:1910.13970, doi: [10.48550/arXiv.1910.13970](https://doi.org/10.48550/arXiv.1910.13970)
- Mao, T.-X., Wang, J., Li, B., et al. 2021, *MNRAS*, 501, 1499, doi: [10.1093/mnras/staa3741](https://doi.org/10.1093/mnras/staa3741)
- Martino, M. C., & Sheth, R. K. 2009, *MNRAS*, 394, 2109, doi: [10.1111/j.1365-2966.2009.14467.x](https://doi.org/10.1111/j.1365-2966.2009.14467.x)
- McCullagh, N., Neyrinck, M. C., Szapudi, I., & Szalay, A. S. 2013, *ApJL*, 763, L14, doi: [10.1088/2041-8205/763/1/L14](https://doi.org/10.1088/2041-8205/763/1/L14)
- Neyrinck, M. C., Szapudi, I., McCullagh, N., et al. 2018, *MNRAS*, 478, 2495, doi: [10.1093/mnras/sty1074](https://doi.org/10.1093/mnras/sty1074)
- Neyrinck, M. C., & Yang, L. F. 2013, *MNRAS*, 433, 1628, doi: [10.1093/mnras/stt949](https://doi.org/10.1093/mnras/stt949)
- Nikakhtar, F., Padmanabhan, N., Lévy, B., Sheth, R. K., & Mohayaee, R. 2023, *PhRvD*, 108, 083534, doi: [10.1103/PhysRevD.108.083534](https://doi.org/10.1103/PhysRevD.108.083534)
- Nikakhtar, F., Sheth, R. K., Lévy, B., & Mohayaee, R. 2022, *PhRvL*, 129, 251101, doi: [10.1103/PhysRevLett.129.251101](https://doi.org/10.1103/PhysRevLett.129.251101)
- Noh, Y., White, M., & Padmanabhan, N. 2009, *PhRvD*, 80, 123501, doi: [10.1103/PhysRevD.80.123501](https://doi.org/10.1103/PhysRevD.80.123501)
- Orban, C., & Weinberg, D. H. 2011, *PhRvD*, 84, 063501, doi: [10.1103/PhysRevD.84.063501](https://doi.org/10.1103/PhysRevD.84.063501)
- Padmanabhan, N., White, M., & Cohn, J. D. 2009, *PhRvD*, 79, 063523, doi: [10.1103/PhysRevD.79.063523](https://doi.org/10.1103/PhysRevD.79.063523)
- Paillas, E., Cai, Y.-C., Padilla, N., & Sánchez, A. G. 2021, *MNRAS*, 505, 5731, doi: [10.1093/mnras/stab1654](https://doi.org/10.1093/mnras/stab1654)
- Paillas, E., Cuesta-Lazaro, C., Zarrouk, P., et al. 2023, *MNRAS*, 522, 606, doi: [10.1093/mnras/stad1017](https://doi.org/10.1093/mnras/stad1017)
- Paillas, E., Ding, Z., Chen, X., et al. 2024, arXiv e-prints, arXiv:2404.03005, doi: [10.48550/arXiv.2404.03005](https://doi.org/10.48550/arXiv.2404.03005)
- Planck Collaboration, Aghanim, N., Akrami, Y., et al. 2020, *A&A*, 641, A6, doi: [10.1051/0004-6361/201833910](https://doi.org/10.1051/0004-6361/201833910)
- Ross, A. J., Samushia, L., Howlett, C., et al. 2015, *MNRAS*, 449, 835, doi: [10.1093/mnras/stv154](https://doi.org/10.1093/mnras/stv154)
- Schmittfull, M., Feng, Y., Beutler, F., Sherwin, B., & Chu, M. Y. 2015, *PhRvD*, 92, 123522, doi: [10.1103/PhysRevD.92.123522](https://doi.org/10.1103/PhysRevD.92.123522)
- Seo, H.-J., Ota, A., Schmittfull, M., Saito, S., & Beutler, F. 2022, *MNRAS*, 511, 1557, doi: [10.1093/mnras/stac082](https://doi.org/10.1093/mnras/stac082)
- Seo, H.-J., Siegel, E. R., Eisenstein, D. J., & White, M. 2008, *ApJ*, 686, 13, doi: [10.1086/589921](https://doi.org/10.1086/589921)
- Seo, H.-J., Eckel, J., Eisenstein, D. J., et al. 2010, *ApJ*, 720, 1650, doi: [10.1088/0004-637X/720/2/1650](https://doi.org/10.1088/0004-637X/720/2/1650)
- Sheth, R. K., & Tormen, G. 1999, *MNRAS*, 308, 119, doi: [10.1046/j.1365-8711.1999.02692.x](https://doi.org/10.1046/j.1365-8711.1999.02692.x)

- Sinha, M., & Garrison, L. 2019, in *Software Challenges to Exascale Computing*, ed. A. Majumdar & R. Arora (Singapore: Springer Singapore), 3–20.  
[https://doi.org/10.1007/978-981-13-7729-7\\_1](https://doi.org/10.1007/978-981-13-7729-7_1)
- Sinha, M., & Garrison, L. H. 2020, *MNRAS*, 491, 3022, doi: [10.1093/mnras/stz3157](https://doi.org/10.1093/mnras/stz3157)
- Villaescusa-Navarro, F., Hahn, C., Massara, E., et al. 2020, *ApJS*, 250, 2, doi: [10.3847/1538-4365/ab9d82](https://doi.org/10.3847/1538-4365/ab9d82)
- von Hausegger, S., Lévy, B., & Mohayaee, R. 2022, *PhRvL*, 128, 201302, doi: [10.1103/PhysRevLett.128.201302](https://doi.org/10.1103/PhysRevLett.128.201302)
- Wang, X., & Pen, U.-L. 2019, *ApJ*, 870, 116, doi: [10.3847/1538-4357/aaf231](https://doi.org/10.3847/1538-4357/aaf231)
- Wang, X., Yu, H.-R., Zhu, H.-M., et al. 2017, *ApJL*, 841, L29, doi: [10.3847/2041-8213/aa738c](https://doi.org/10.3847/2041-8213/aa738c)
- White, M. 2010, arXiv e-prints, arXiv:1004.0250, doi: [10.48550/arXiv.1004.0250](https://doi.org/10.48550/arXiv.1004.0250)
- . 2015, *MNRAS*, 450, 3822, doi: [10.1093/mnras/stv842](https://doi.org/10.1093/mnras/stv842)
- Yu, Y., Zhu, H.-M., & Pen, U.-L. 2017, *ApJ*, 847, 110, doi: [10.3847/1538-4357/aa89e7](https://doi.org/10.3847/1538-4357/aa89e7)
- Zarrouk, P., Burtin, E., Gil-Marín, H., et al. 2018, *MNRAS*, 477, 1639, doi: [10.1093/mnras/sty506](https://doi.org/10.1093/mnras/sty506)
- Zhao, C., Chuang, C.-H., Kitaura, F.-S., et al. 2020, *MNRAS*, 491, 4554, doi: [10.1093/mnras/stz3339](https://doi.org/10.1093/mnras/stz3339)